Methane steam reforming on Ni@Pt catalyst: combined DFT and experimental kinetic study

Juntian Niu[a,b], Yalan Wang[b], Yanying Qi[b], Anh H. Dam[b], Hongmin Wang[b], Yi-An Zhu[c], Anders Holmen[b], Jingyu Ran[a*], De Chen[b*]

[a] Key Laboratory of Low-grade Energy Utilization Technologies and Systems, Ministry of Education of PRC, Chongqing University, Chongqing, 400044, China

[b] Department of Chemical Engineering, Norwegian University of Science and Technology, Trondheim, 7491, Norway

[c] State Key Laboratory of Chemical Engineering, East China University of Science and Technology, Shanghai, 200237, China

*Corresponding authors: De Chen and Jingyu Ran

E-mail: de.chen@ntnu.no; ranjy@cqu.edu.cn

Abstract: In this contribution, we combine density functional theory (DFT) calculations, experimental kinetic study and DFT assisted kinetic analysis to elucidate the impact of the interface of monolayer Pt on the Ni surface on catalytic performance of steam methane reforming including carbon formation on core-shell (Pt@Ni) catalysts and compare to Ni and Pt catalysts. We demonstrate experimentally that core-shell structured Pt@Ni significantly lowers the carbon formation without scarifying much the activity. The DFT results demonstrate that the metal identity, core shell structure and support have significant impacts on the reaction mechanism. The direct methane activation is energetically favorable reaction pathway on Ni, while the OH* assisted methane activation is the favorable pathway on Pt and Pt@Ni catalysts, where methane activation is the rate-determining step on all catalysts. We unambiguously reveal that the core-shell Ni@Pt catalyst modified the surface Pt electron density and shifted d-band center away from Fermi level compared with Ni(111) and Pt(111), which could lead to weakening the binding strength of absorbates on metal surface. It resulted in a strong base of surface OH* which actively reacts with CH_x and thus enhance carbon formation resistance. From the free energy profile based on DFT-calculated energetics, a kinetic model is constructed, and the determined effective activation barriers agree well with the experimental measured ones. By taking into account the activation of steam on the support and modifying the entropy changes of the methane activation, the kinetic model can describe the experimental kinetic performance satisfactorily.

Keywords: CH_4/H_2O reforming; OH-assisted activation; Coke formation; Kinetic study; Ni@Pt

1. Introduction

Due to the massive available in natural gas and shale gas reserves, the catalytic activation and conversion of methane is of great interest both in the catalytic community and industrial application [1–3]. This reaction is involved in some important chemical processes, such as methane total oxidation [4,5], methane partial oxidation [6,7], steam reforming of methane (*SRM*) [8,9] and dry reforming of methane (*DRM*) [10,11]. Above all, *SRM* plays a key role in the large scale of production of syngas and hydrogen from natural gas. The Ni-based catalysts are considered as a promising candidate due to their low cost and high activity [12,13]. However, carbon deposition is a serve problem for Ni catalysts, which would lead to a destruction of catalysts and reactor as well as rapid deactivation [14] due to coke formation [15]. Single component Ni catalysts hardly meet the activity and stability demands.

Noble catalysts have been found to be much more resistant to carbon deposition than Ni catalysts [16,17]. However, large scale application remains challenge due to their high prices. Manipulating the metal size and composition in nano-catalysis paves the way to improve the catalytic performance and replace and/or lower the precious metal usage. Bimetallic catalysts and core-shell structure are feasible and effective way to tune chemical and electronic properties on purpose [18]. However, most catalysts with better carbon resistant in methane reforming compensated by a lower activity [19,20]. Decoupling the catalysts activity and stability to develop catalysts with high activity, selectivity and stability simultaneously remains a formidable challenge. The core-shell nanoparticle is found to be an effective approach to design highly active, stable and low-cost materials with high noble metal utilization for both thermo- and electro-catalysis [21]. Such core-shell offers the promise of ultralow precious metal loadings while non-precious transition metal cores hold the promise of thermodynamic stability and access to unique catalytic activity, such as designing core-shell nanocatalysts in hydrocarbon reforming reactions for syngas production to reach high

stability [22–24].

Density functional theory (DFT) combined microkinetic modeling has gained an increasing attention in exploring mechanistic insights and catalyst rational design. Through the first-principles study, Huang et al. [25] suggested to increase resistant to carbon formation by lowing methane dissociation activity through Au/Ni surface alloys. Similarly surface alloying of Rh [26] with Ni(100) and alloying of Pd [27] as well as Au [28] with Ni(111) have been found to reduce the methane dissociation and thus reduce the carbon potential. The results showed that Pt-doped Ni(111) [29] surface is beneficial to the adsorption of CH_x and H species. Moreover, Fan et al. [30] studied the origin of synergistic effect over Ni-based bimetallic surfaces (NiM; M = Cu, Ru, Rh, Pd, Ag, Pt and Au) for methane dissociation. The results proved that Pt-promoted Ni catalyst shows the best coke resistance.

Moreover, David and Matthew work [31] has reported that absorbed O* and OH* could withdraw electron density from the surface to form a negatively charged surface intermediates that serve as a Brønsted base [32,33], which can activate C–H bond during the oxidation and oxidative dehydrogenation reactions [32]. On Pt(111) surface very similar barriers was found for OH*-assisted and direct CH_4 activation. Thus, Pt surface can possibly be manipulated to significantly reduce the activation barrier of methane. In addition, core-shell nanoparticles have been gaining increasing interests to improve the catalytic performance through introducing the strain to modify the electronic properties [24,34,35]. Ni-core/Pt-shell particle was found to be a stable structure due to a moderate surface segregation energy of Pt on Ni [36], thus providing a promising candidate for oxidation–reduction reactions [37] to decouple the catalyst activity and stability.

Here we report that Ni-core/Pt-shell particle (Ni@Pt) decouples the activity and carbon resistance to keep the activity and reduce carbon formation simultaneously in methane steam reforming. A systematical DFT study of methane activation by O* and OH* assisted

activation as well as direct deprotonation and CH_x oxidation on Ni@Pt is performed and compared to Ni(111) and Pt(111) surface. Reaction pathways are elucidated and their dependence on the surfaces is revealed. We unambiguously reveal that the core-shell Ni@Pt catalyst modified the surface Pt electron density and lowered the adsorption strength of intermediates, which resulted in a strong base of OH* to actively react with methane and CH_x and enhance carbon formation resistance without scarifying the reaction activity. In addition, we have performed the kinetic study over Ni and Ni@Pt catalysts in *SRM* to compare and validate the DFT results. Temperature programmed oxidation (TPO) analysis for the catalysts after reaction was tested to obtain the coke formation rate and compare with the coke potential drawn from DFT predictions.

2. Computational and experimental details

2.1 Computational models

The (111) surface usually dominates the surfaces of metal nanoparticles [38], so pure Ni(111) and Pt(111) as well as Ni@Pt are chosen as the reaction surfaces in this paper. Based on the optimized pure Ni bulk and Pt bulk, the five atomic layers Ni(111) and Pt(111) surface models were built. The bottom two layers were fixed at their equilibrium bulk positions, and the top three layers and the adsorbates were allowed to relax. Additionally, a p(3 × 3) supercell was applied, with a coverage of adsorbates of 1/9 ML, which has been widely used in previous DFT study dealing with molecular interactions with metal surfaces [12]. The computational method results in a self-consistent lattice constant of 3.540 Å (*3.52* Å [8]) for the Ni bulk and 3.982 Å (*3.92* Å [39]) for the Pt bulk, respectively, which are in good agreement with the well accepted experimental value in the bracket. Ni@Pt core-shell surface was built based on the optimized Ni(111) by substituting first layer Ni atoms into Pt atoms. The metal (111) surfaces are provided in Fig. 1.

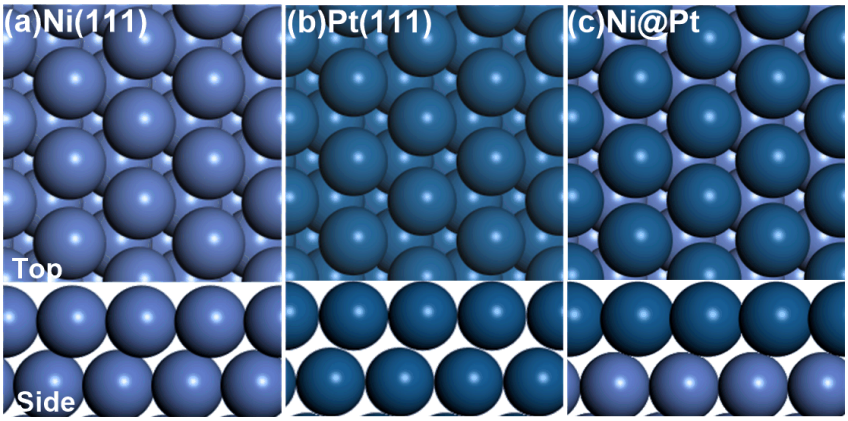

Fig. 1. Three surface models (a) Ni(111); (b) Pt(111); and (c) Ni@Pt.

2.2 Density functional theory (DFT) calculations

All the DFT calculations were conducted with a periodic slab model using the Vienna ab initio simulation program (VASP) [38,40]. All calculations were conducted with the generalized gradient approximation (GGA) and the Bayesian error estimation functional with van der Waals correlation (BEEF-vdW) [41], which was developed to address van der Waals interaction reasonably at an accurate description of adsorption energies of molecules on surfaces [42]. In addition, BEEF-vdW works most satisfactorily among the selected functional since it has the smallest mean absolute error by comparing results from different functions such as BEEF-vdW, RPBE, and PBE with a database of 30 adsorption reaction energies [43]. Projector augmented wave (PAW) method was used to describe the electrons-ion interaction [44]. And the plane wave cutoff energy of 400 eV was utilized in the calculation of the compact convergence. DFT calculations considered spin-polarized electrons for Ni(111) and Ni@Pt surfaces, which account for the magnetic moment of Ni. A 15 Å vacuum region was used to ensure the intermolecular interaction between the slabs was negligible. In addition, a Fermi smearing of 0.2 eV was applied in our present work. Brillouin zone integration was approximated by a sum over special k-points chosen using the Monkhorst–Pack method [45]. The meshes of 5 × 5 × 1 k-points for the Ni(111), Pt(111) and Ni@Pt surfaces.

Moreover, transition states were searched by dimer method [46]. All the optimizations are converged with a force criterion of 0.03 eV/Å. The transition states in this work were verified by frequency analysis, and only one imaginary frequency was identified for each transition state, the details is provided in Supporting Information Table S1.

The adsorption energy of the adsorbate is given by:

$$E_{ads} = E_{adsorbate/surface} - E_{adsorbate} - E_{surface} \quad (1)$$

where $E_{adsorbate/surface}$ is the total energy of the surface with the adsorbate adsorbed, $E_{adsorbate}$ is the total energy of the isolated adsorbate, and $E_{surface}$ is the total energy of the bare surface. A negative value for the adsorption energy indicates that the adsorption process is exothermic.

The activation barrier (E_a) of forward reaction is given by:

$$E_a = E^{TS} - E^{IS} \quad (2)$$

where E^{TS} is the total energy of transition state, and E^{IS} is the total energy of initial state.

The reaction heat (ΔH) of an elementary reaction is given by:

$$\Delta H = E^{FS} - E^{IS} \quad (3)$$

where E^{FS} is the total energy of final state.

2.3 Thermodynamic analysis

All the thermodynamic properties were calculated at a temperature of 1000 K firstly. Moreover, 773 K, 798 K, 823 K and 848 K applied for kinetic relevant steps to compare with the experimental results. The Gibbs free energy (G) of gas phase species was estimated by taking into account transitional, rotational and vibrational contributions. For the surface adsorbed species, only vibrational contribution was considered, including zero-point energy (ZPE), vibrational thermal energy and vibrational entropy [14, 20]. The standard molar Gibbs free energy for each species in methane dehydrogenation and reforming is calculated as [14]:

$$G^0 = E_{\text{total}} + E_{ZPE} + \gamma RT(1+In\frac{P}{P^0}) + U^0 - TS^0 \quad (4)$$

where E_{total} is the total energy obtained from DFT calculations, and E_{ZPE}, U^0 and S^0 are the correction energy from ZPE, thermal energy and entropy, respectively. R is the gas constant, P is the partial pressure of the gas-phase molecule, γ is 0 for the surface adsorbed species and 1 for gaseous molecule.

2.4 Catalyst preparation

Monometallic 12wt% Ni derived from hydrotalcite-like precursor has been prepared by co-precipitation using metal nitrites component, keeping the ratio of Ni:Mg:Al at 0.37:2.63:1 . Ni@Pt catalysts were prepared by redox reaction of the reduced Ni catalyst with the modifiers Pt in solution in the form of a precursor salt at ambient temperature. During the redox reaction, Ni atoms were gradually substituted into Pt atoms on the surface of Ni particles and Ni^{2+} formed accordingly, $Pt^{2+} + Ni \rightarrow Pt + Ni^{2+}$.

2.5 Catalyst characterization

In order to determine the specific surface area of nickel and nickel alloying, measurements of H_2 chemisorption were performed on a Micromeritics ASAP 2010C unit at 308 K. 200 mg of the freshly calcined catalysts were loaded in tubular quartz reactor, evacuated at 308 K for 1 h and reduced in a 5% H_2/He flow at 943 K for 10 hrs. in a quartz micro-reactor. After reduction, the sample was evacuated for 0.5 hrs. at 943 K and for 1 h at 308 K. At this temperature, an adsorption isotherm was recorded and the metal dispersion was determined according to the quantity of hydrogen uptake.

The X-ray photoelectron spectroscopy (XPS) analyses were performed, where a monochromatized Al Kα X-ray source (GammaData Scienta) was used to get the exciting radiation in a hemispherical SCIENTA SES 2002 electron energy analyzer. The total energy resolution for XPS was estimated to be about 0.4 eV. All spectra were measured in angle integrated mode around normal emission. Transmission electron scanning (TEM) images were taken and analyzed using a JEOL-2010F, with an accelerating voltage of 200 kV. The

samples were prepared by ultrasonic dispersion of the reduced catalysts in ethanol. Drops of samples were put on a copper grid supported with a carbon film.

2.6 Methane reforming

Kinetic study of methane steam reforming was performed in a fixed-bed reactor at atmospheric pressure. The catalyst bed consisted of 10 mg of Ni catalyst (50-150 μm) diluted with inert α-Al_2O_3 (100 mg). Product concentrations were measured online with a micro-gas chromatograph. The catalysts were heated from room temperature to 670 °C at 2 °C/min in a mixture of 1/1 H_2/Ar (total flow of 200 cm^3/min) and held at these conditions for 12 h reduction. The temperature dependence was S/C=3.5, and, CH_4/H_2=1.0 where the W/F_0 was varied to control the conversion lower than 10%. In addition, stability test was performed at S/C=1 at 700 °C, 1 atm. Coke formation on spent catalysts was investigated by a TGA-MS (TGA: Netzsch STA 449C Jupiter, MS: Netzsch Aërlos QMS 403C) system under an Air/Helium (90/10 ml•min^{-1}) atmosphere, heating from ambient temperature to 900 °C, at a ramping rate of 10 °C/min, and dwelling for half hour at this temperature. The amount of coke formation was estimated by the mass loss in TGA analysis, confirming by MS results.

3. Results and discussion

3.1 Reaction network for methane steam reforming

A reaction network for methane steam reforming considered in this work is provided in Fig. 2. The whole reaction network is separated into five parts, specifically, it consists of CH_4 dissociation, H_2O dissociation, CH oxidation, C oxidation and H_2 formation, respectively. Three pathways of CH_4 activation, namely direct dissociation, O-assisted and OH-assisted activation, respectively, have been taken into account. In terms of H_2O dissociation, the H_2O molecule direct dissociation into OH and H is considered. As for CH oxidation, O and OH assisted pathways have been taken into account. The intermediates of CHO, COH, CHOH are

formed in the CH oxidation processes and the details are shown in the CH oxidation part of Fig. 2. In addition, C is oxidized by O and OH, and the target product of both CH and C oxidation is CO. H_2 is generated from absorbed H atoms on the surface.

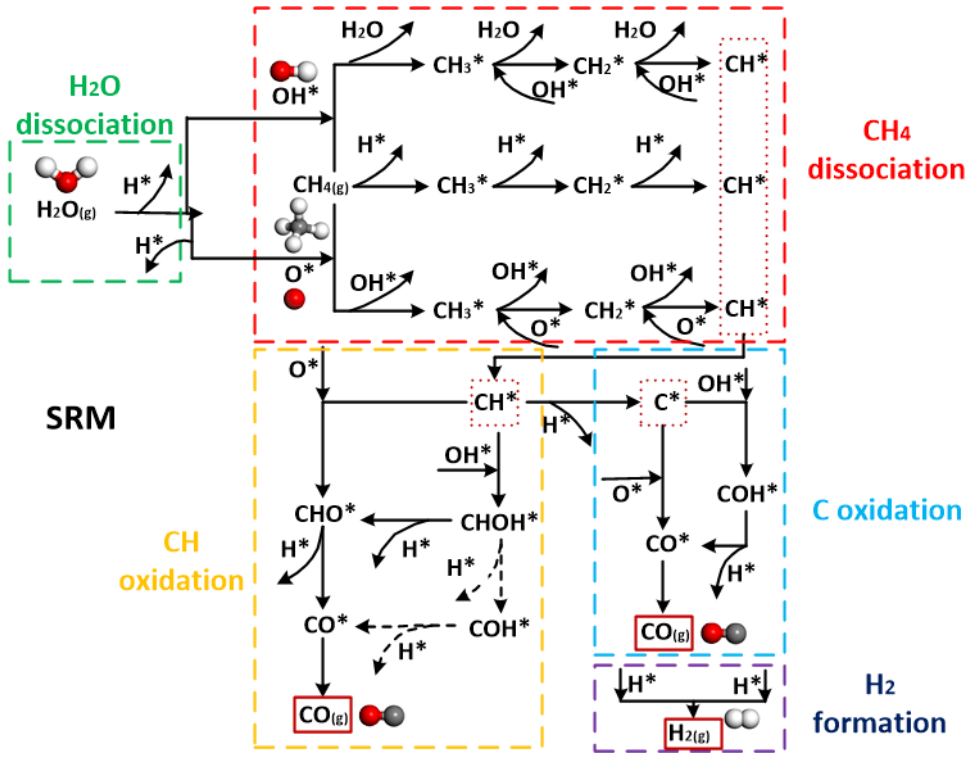

Fig. 2. Reaction network for methane steam reforming considered in this work. The whole network is divided into five parts: H_2O dissociation (in dashed green rectangle), CH_4 dissociation (in dashed red rectangle), CH oxidation (in dashed orange rectangle), C oxidation (in dashed light blue rectangle) and H_2 formation (in dashed dark blue rectangle).

3.2 Projected density of states (PDOS) and adsorption of main species

Fig. 3a shows the projected density of states for *d* orbital on three metal surfaces, it is found that introducing Pt atoms into Ni surface forming Ni@Pt makes the curves of PDOS broader and *d*-band center shifted away from Fermi level compared with Ni(111) and Pt(111), which could lead to weakening the binding strength between absorbates and metal surface. The corresponding *d*-band center of three metal surfaces is calculated to be – 1.31 eV [Ni(111)], – 2.00 eV [Pt(111)], and – 2.59 eV [Ni@Pt], respectively.

According to adsorption energy of species provided in Table S2, some features could be

drawn. Above all, the binding energies on the Ni@Pt surface are the weakest among three surfaces, which is in good agreement with *d*-band center of metal surface. Additionally, Pt(111) shows the strongest binding energy for most species, except for O*, H*, OH* and CO*. Specifically, as for C*, the lowest adsorption energy occurs on Ni@Pt surface, indicating that C* on Ni@Pt is more easier to react with other species, such as O*/OH*, which could lead to less carbon formation on the surface compared with Ni(111) and Pt(111). In terms of O*, there is a big difference among three surfaces, the binding energies are – 5.21eV [Ni(111)], – 4.04 eV [Pt(111)], and – 3.09 eV [Ni@Pt], respectively. For H*, the binding energy on the Ni@Pt is lower than the others, suggesting that H_2 is easier to form. In addition, the most favored adsorption site on Ni(111) and Pt(111) is hollow site for OH*, while it moves to top site on the Ni@Pt surface with the lowest binding energy. Therefore, OH-assisted dehydrogenation becomes a possible way on Ni@Pt surface, which will be discussed later. CO is one of dominant products in this reaction, binding ability on the Ni@Pt is the weakest and CO* is more favored to desorb into gas phase on this surface.

Fig. 3b displays the main chemisorbed species involved in methane activation and reforming reactions. In conclusion, Ni(111) shows the best ability of binding oxygen atom of oxygenated species among the three surface and Pt(111) has the highest binding energy for carbon atom of hydrocarbon species, while Ni@Pt lower the adsorption of both C and O contained intermediates. In addition, strong adsorption could promote reactant initial dissociation, while weak adsorptive species is easier to join in the surface reaction, so a good catalyst for this process should have moderate adsorption strength for reactive species.

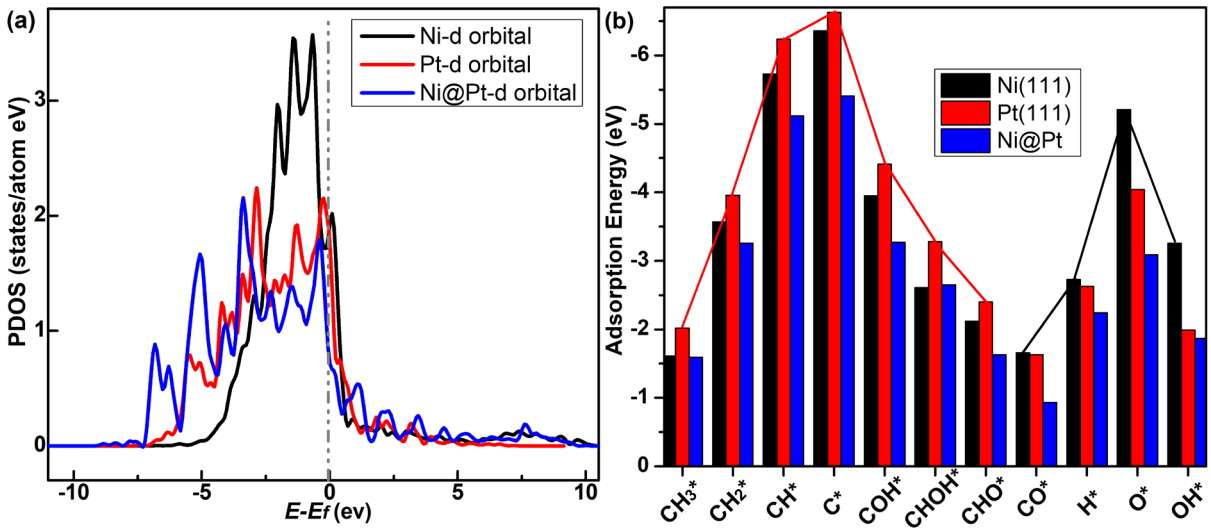

Fig. 3. (a) Projected density of states for *d* orbital; and (b) Main chemisorbed species on three metal surfaces. The dash line donates the Fermi level.

3.3 DFT study of CH_4/H_2O reforming

Table 1 provides the activation energy (Ea) and reaction heat (ΔH) in CH_4/H_2O reforming on Ni(111), Pt(111) and Ni@Pt, respectively. The detailed discussion will be presented in the following sections.

Table 1

Activation energy (E_a) and reaction heat (ΔH) in methane activation and reforming on Ni(111), Pt(111) and Ni@Pt.

	Ni(111)		Pt(111)		Ni@Pt	
	E_a	ΔH	E_{ads}	ΔH	E_{ads}	ΔH
CH_4 direct dissociation (A)						
$CH_4 + 2^* \leftrightarrow CH_3^* + H^*$	1.206	0.545	1.033	0.217	1.725	1.084
$CH_3^* + ^* \leftrightarrow CH_2^* + H^*$	0.874	0.334	1.032	0.499	1.544	1.061
$CH_2^* + ^* \leftrightarrow CH^* + H^*$	0.434	– 0.158	0.518	– 0.191	1.224	0.732
$CH^* + ^* \leftrightarrow C^* + H^*$	1.445	0.643	1.617	0.996	1.979	1.545
O*/OH* assisted CH_4 activation (B)						
$CH_4 + O^* + ^* \leftrightarrow CH_3^* + OH^*$	1.661	0.537	1.552	– 0.119	1.424	– 0.332
$CH_4 + OH^* \leftrightarrow CH_3^* + H_2O$	3.389	0.859	0.699	– 0.777	1.191	– 0.455
$CH_3^* + O^* \leftrightarrow CH_2^* + OH^*$	1.565	0.573	1.618	0.227	1.356	– 0.229
$CH_3^* + OH^* \leftrightarrow CH_2^* + H_2O + ^*$	0.931	0.58	1.068	– 0.293	1.191	– 0.406
$CH_2^* + O^* \leftrightarrow CH^* + OH^*$	1.023	– 0.093	1.582	– 0.446	1.011	– 0.636
$CH_2^* + OH^* \leftrightarrow CH^* + H_2O + ^*$	0.865	– 0.145	0.662	– 0.953	0.619	– 1.02
H_2O dissociation (C)						

$H_2O^*+ * \leftrightarrow OH^* +H^*$	1.003	– 0.186	0.913	0.795	1.539	1.517
$OH^*+ * \leftrightarrow O^* +H^*$	1.311	0.091	0.768	0.037	1.851	1.207
CH and C oxidation (D)						
$CH^* + O^* \leftrightarrow CHO^* + *$	1.134	0.406	1.29	– 0.908	0.739	– 1.965
$CHO^* + * \leftrightarrow CO^* + H^*$	0.256	– 0.986	0.474	– 0.566	0.562	– 0.204
$CH^* + OH^* \leftrightarrow CHOH^* + *$	1.162	0.731	0.800	0.228	0.596	– 1.305
$CHOH^* + * \leftrightarrow CHO^* + H^*$	0.540	– 0.302	0.184	– 0.105	0.84	0.609
$CHOH^* + * \leftrightarrow COH^* + H^*$	1.515	– 0.155	1.612	– 0.305	1.482	0.773
$COH^* + * \leftrightarrow CO^* + H^*$	1.071	– 0.954	1.075	– 0.265	1.157	– 0.281
$C^* + O^* + * \leftrightarrow CO^* + *$	1.300	– 1.723	1.354	– 2.406	0.902	– 3.774
$C^* + OH^* \leftrightarrow COH^* + *$	1.141	– 0.605	0.729	– 1.645	0.396	– 2.17
C formation (E)						
$CH^* + * \leftrightarrow C^* + H^*$	1.445	0.643	1.617	0.996	1.979	1.545
$COH^* + * \leftrightarrow C^* + OH^*$	1.746	0.605	2.374	1.645	2.566	2.17
$CO^* + * \leftrightarrow C^* + O^*$	3.023	1.723	3.76	2.406	4.676	3.774
CH consumption (F)						
$CH^* + * \leftrightarrow C^* + H^*$	1.445	0.643	1.617	0.996	1.979	1.545
$COH^* + * \leftrightarrow C^* + OH^*$	1.746	0.605	2.374	1.645	2.566	2.17
$CO^* + * \leftrightarrow C^* + O^*$	3.023	1.723	3.76	2.406	4.676	3.774

3.3.1 CH_4 direct activation

Methane is a quite stable molecule owing to its large C–H bond energy and strictly symmetrical structure. Generally, the activation of first C–H bond was found to be the rate-limiting step in methane activation and reforming reactions [20,47]. Now that CH_4 direct activation to form surface C and H is investigated on three surface. The activation energy and reaction heat in this process are listed in Table 1A. Additionally, Fig. S1 presents top views and side views (insets) of transition states of CH_4 direct successive dehydrogenation.

For the first step of CH_4 dehydrogenation, Ni@Pt shows the highest barrier among the three surfaces with a value of 1.725 eV, and also it is a strong endothermic step, indicating that CH_4 direct dissociation is difficult to proceed on this surface. The CH_4 activation energy for Ni(111) is 1.206 eV, which is close to the reported values (1.18 [48], 1.21 [49], 1.23 [50]), and for Pt(111) is 1.033 eV, in good agreement with previous literature 1.06 eV from GGA/rPBE functions [31], both of them are lower than that of Ni@Pt. As for CH_x(3-1)

dehydrogenation, the activation energy on different catalysts follows an order of the CHx adsorption heat, namely Ni(111) < Pt(111) < Ni@Pt. The activation barrier of CH dissociation on Ni@Pt remarkably increases to 1.979 eV, especially higher than that on Ni(111), suggesting that Ni@Pt structure has promising anti-carbon formation ability.

In conclusion, this process is hard to proceed on Ni@Pt surface from both kinetically and thermodynamically, due to the large activation barrier and strong endothermic property. In addition, Ni(111) and Pt(111) have similar dehydrogenation ability for CH_4. Specifically, Pt(111) shows a little better catalytic performance for methane dissociation than Ni(111), meanwhile, it enhances barrier for last dehydrogenation step, indicating that Pt metal has better anti-carbon formation ability, which is proved in both DFT calculations [49,51] and experimental work [52,53].

3.3.2 O*/OH*assisted activation of CH_4

O* assisted and OH* assisted C–H of CH_4 activation paths proceeding via reductive deprotonation over the metal-O* or metal-OH* site pairs [31–33] have been investigated here to compare with direct dissociation. The adsorbed O* and OH* serve as base sites which attack the acidic bond C–H bond in CH_4. The activation energy of CH_4 dissociation follows an order of Ni@Pt < Pt(111) <Ni(111), which is an inverse order of O* and OH* binding energy, respectively. The CH_4 activation is more favorable to proceed under the assistance of OH* than that with O* assisted and direct dissociation ways on Ni@Pt. The binding energy of OH* on Ni(111) which behaves a relatively weak base, resulted in a high activation energy for first C–H bond activation of CH_4. In contrast, the strain introduced by the core-shell structure lowered the OH* binding energy. Therefore, Ni@Pt surface possesses the lowest activation energy for CH_4 activation. For the O* and OH* assisted CH_x* activation, it follows the order of the reaction heat, while the presence of OH* largely inhibits first C–H bond dissociation of CH_4 on Ni(111), which could be attributed to the strong binding energy for

OH on Ni(111) surface and large entropy loss in gas phase CH_4 adsorptive dissociation process. For the following dehydrogenation processes, the OH* assisted pathway is superior to O* assisted way on all three surfaces, indicating that OH* species could promote most of dehydrogenation steps on three metal surfaces, except first C–H bond activation of CH_4 on Ni(111). The activation energy and reaction heat are listed in Table 1B. Moreover, Fig. S2 presents top views and side views (insets) of transition states of CH_4 dissociation through O* and OH*.

In conclusion, as for the activation of first C–H bond of CH_4 on three metal surfaces, direct dissociation into CH_3* and H* proceeds more easily on Ni(111) than O* and OH* assisted CH_4 activation. However, compared with barrier of direct dissociation, the barriers of OH* assisted CH_4 activation are decreased by 0.334 eV on Pt(111) and 0.534 eV on Ni@Pt, respectively. Thus, OH-assisted CH_4 activation in reforming process becomes an attractive alternative route on Pt(111) and Ni@Pt surface.

3.3.3 H_2O dissociation

H_2O dissociation on three surfaces is comparatively studied. The stable configurations for H_2O binding on the three models are all at the top site with the molecular plane almost parallel to the surface. Table 1C gives the activation energy and reaction heat of H_2O dissociation. In addition, Fig. S3 displays the top views and side views (insets) of transition states in H_2O dissociation. For the initial H_2O dissociation into OH* and H*, the Ni(111) and Pt(111) show the similar activation barrier close to 1 eV, which has been reported in former literature [57], while this step requires a higher barrier on Ni@Pt surface with a value of 1.539 eV. Most of previous works focus on H_2O initial dissociation step. As for the OH* further decomposition into O* and H*, Ni(111) shows the best performance, contrarily, Ni@Pt has a much higher energy barrier.

In order to see thermodynamic and kinetic details in H_2O dissociation, energy profiles

for H_2O dissociation on three surfaces are plotted. As seen from Fig. S4, both OH* and O* are possible to form in H_2O dissociation on Ni(111), while it becomes less favored to complete the OH* decomposition step on Pt(111) and Ni@Pt surface, especially for Ni@Pt, this step is almost impossible to proceed. As a consequence, OH* is the dominant product of H_2O dissociation on Pt(111) and Ni@Pt, while this process could provide both OH* and O* species as oxidant for CH_x activation on Ni(111) surface.

3.3.4 CH and C oxidation

According to the previous report [18], CH is the most abundant species in methane dehydrogenation process on Pt(111) surface. Zhu et al. [47] found that only the CH oxidation and C oxidation are likely to proceed on Ni(111) surface, and also the pathway of CH oxidation is more favorable. However, CH and C oxidation pathways on Ni@Pt surface are still unknown, and the systematical comparison of reaction pathways on three surfaces are lacking.

All the activation energy and reaction heat in the CH and C oxidation on three metal surfaces are listed in Table 1D. As seen from table, it could be concluded that the stronger adsorption strength between the carbon/oxygen and surface are, the higher barrier for the C and CH oxidation in the reaction. The energy barriers for CH and C oxidation through oxygen are according to the following sequence: Pt(111) > Ni(111) > Ni@Pt, which is consistent with the tendency of carbon adsorption energy, while through hydroxyl assisted oxidation way for CH and C, the activation barriers follow the order: Ni(111) > Pt(111) > Ni@Pt, which has the same trend with the oxygen binding energy. In conclusion, no matter the O* or the OH* assisted oxidation of both CH and C, the Ni@Pt surface always shows the lowest energy barrier for these processes, thus Ni@Pt is predicted to be a good candidate in the reaction of CH and C oxidation. Moreover, Fig. S5 describes the top views and side views (insets) of transition states of CH and C oxidation on three surfaces.

Fig. S6 shows the energy profiles for CH oxidation by both O* and OH* assisted ways on three surfaces. As for O* assisted CH oxidation way, it forms the intermediate of CHO* species firstly, Ni@Pt shows the lowest energy barrier for this process. Then CHO* dissociates into CO* and H*, the low barrier and enthalpy decrease for the CHO* dissociation suggest that CHO is not a stable intermediate on these surfaces, which has been mentioned in former work [14]. In summary, the Ni@Pt has the lowest energy barrier for CH* oxidation into CO* and H* through absorbed oxygen atoms. On the other hand, regarding the OH* assisted oxidation of CH, the intermediate CHOH* appears in the beginning, in the CHOH* forming step, it is found that Ni@Pt still presents the lowest energy barrier. Then, CHOH* decomposes into CHO* or COH*, the former way proceeds more easily than the latter on all three surfaces in this work, which is in good agreement with previous studies [18,39,58]. Therefore, Ni@Pt surface exhibits the best performance for the oxidation of CH* into CO* and H* by absorbed hydroxyl. The energy barrier for CH* oxidation through OH* follows the order: Ni(111) > Pt(111) > Ni@Pt. As a result, Ni@Pt model presents the better ability for CH* oxidation through both O* and OH* assisted ways, compared with Ni(111) and Pt(111).

Fig. S7 presents the energy profiles for C oxidation by both O* and OH* assisted ways on three surfaces. As for surface carbon oxidation through O*, it directly goes into CO*, while for OH* assisted way, it forms intermediate COH* firstly, and then COH* splits into CO* and H*. The most favored path for both C + O and C + OH reactions happens on Ni@Pt surface, the activation barriers are 0.902 eV and 0.396 eV respectively, indicating that carbon oxidation is accelerated on the Ni@Pt and this surface is predicted to have good performance for carbon elimination. The energy barriers of C + OH reaction on three surfaces are all lower than the corresponding values of C + O reaction, indicating that OH species is more effective for carbon elimination than O species, which has been reported in previous literature [59].

3.3.5 Carbon formation

Three major reaction paths for carbon formation have been considered in this work, which are CH* decomposition into C* and H*, COH* dissociation into C* and OH*, CO* cracking into C* and O*, respectively. The activation energy and reaction heat are provided in Table 1E. It is found that CH decomposition is the most favorable way for carbon formation on all surfaces. Furthermore, Fig. S8 presents the energy profiles for C formation on three surfaces, the barrier for CH cracking on Ni@Pt is the highest among the three surfaces with a value of 1.979 eV, suggesting that surface carbon is hard to form on this surface, thus Ni@Pt has good anti-carbon ability in methane dehydrogenation and reforming reactions.

As mentioned above, CH cracking reaction is the most possible reaction way for carbon formation on three surfaces. To further investigate the possibility for CH decomposition on different surfaces, the competitive pathways of CH oxidation through O* and OH* have been taken into comparison. Table 1F gives the activation energy and reaction heat in these processes. If the proper amount of O* or OH* can be supplied during the reaction, the oxidation pathways of both O* and OH* assisted show a lower activation barrier for CH consumption, especially for OH* assisted oxidation. Moreover, energy profiles for CH consumption on three metal surfaces is shown in Fig. S9, Ni@Pt surface has the largest Ea difference between the CH decomposition and oxidation through OH*, suggesting that CH prefers to be oxidized rather than cracking into surface carbon.

On the one hand, carbon is difficult to form from CH cracking reaction on Ni@Pt, even if a small amount of carbon deposition is accumulated during in the reaction on this surface, it could be easily oxidized into CO* and COH*, which has been demonstrated in the former C oxidation sections. In conclusion, we propose a descriptor of carbon formation possibility, from two sides of CH cracking into surface carbon possibility and the ability of surface

carbon to be oxidized. Table 2 provides the Ea difference between CH decomposition and oxidation through O* and OH*, respectively, and also gives the barrier for surface carbon oxidation on three catalyst models. According to the results and discussion, we plot the relationship between carbon formation possibility and related reaction barriers, as depicted in Fig. 4. We define the C oxidation barrier from Ea (C+O/OH ↔ CO/COH), and CH oxidation ability from [Ea(CH ↔ C + H) – Ea(CH+O/OH ↔ CHO/CHOH)]. And we assume that the center lever of total rectangular region on each surface represents the possibility of carbon formation. From both O* and OH* assisted oxidation pathways, Ni@Pt always keeps the lowest center lever of total rectangular region. Consequently, Ni@Pt model shows the lowest possibility of surface carbon formation in methane dehydrogenation and reforming reactions.

Table 2

Ea difference between CH decomposition and oxidation through O* and OH*, and barriers for surface carbon oxidation on three catalysts.

	Ni(111)	Pt(111)	Ni@Pt(111)
$Ea_{(CH \leftrightarrow C + H)} - Ea_{(CH+O \leftrightarrow CHO)}$	0.311	0.327	0.629
$Ea_{(CH \leftrightarrow C + H)} - Ea_{(CH+OH \leftrightarrow CHOH)}$	0.283	0.817	1.383
$Ea_{(C+O \leftrightarrow CO)}$	1.300	1.354	0.902
$Ea_{(C+OH \leftrightarrow COH)}$	1.141	0.729	0.396

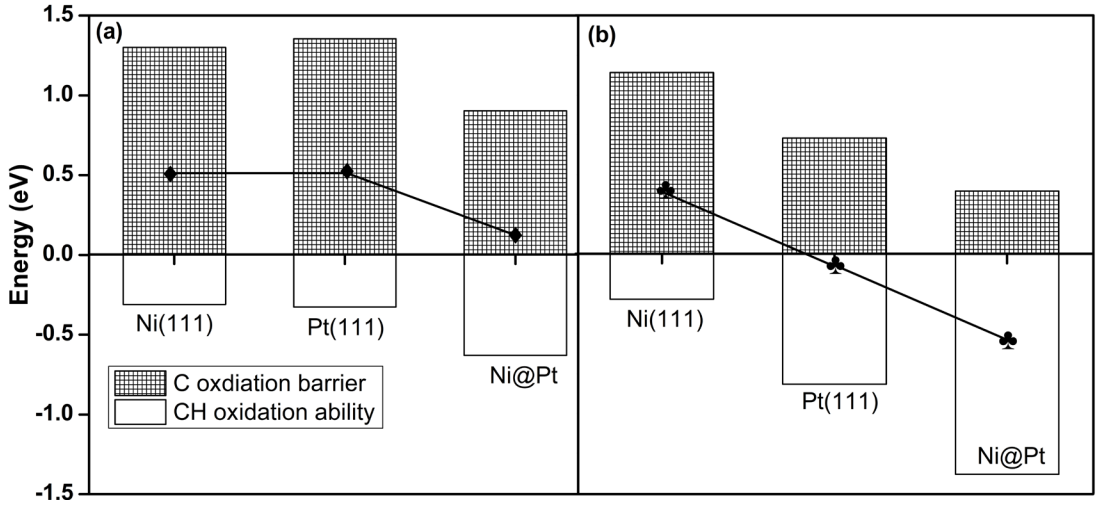

Fig. 4. Carbon formation possibility from both (a) O* and (b) OH* assisted ways on three surfaces. C oxidation barrier: Ea (C+O/OH ↔ CO/COH); CH oxidation ability: Ea(CH ↔ C + H) – Ea(CH+O/OH ↔

CHO/CHOH).

3.3.6 H_2 and CO formation

For the H_2 formation from adsorbed H atoms, the barrier on Ni@Pt is the lowest among the three surfaces with a value of 0.361 eV. In addition, this process is exothermic on Ni@Pt, while is endothermic on the other two surfaces. The exothermic reaction with low activation barrier suggests that H_2 is much easier to form on Ni@Pt surface. Energy profiles for H_2 formation on three surfaces are shown in Fig. 5a. CO is the other dominant final product in methane dehydrogenation and reforming process. The CO adsorption site and adsorption heat are shown in Fig. 5b. Compared with the Ni(111) and Pt(111) surface, the lowest CO adsorption heat occurs on Ni@Pt, indicating that CO is more likely to desorb on this surface. Therefore, the Ni@Pt structure is a good catalyst candidate beneficial for both H_2 and CO formation.

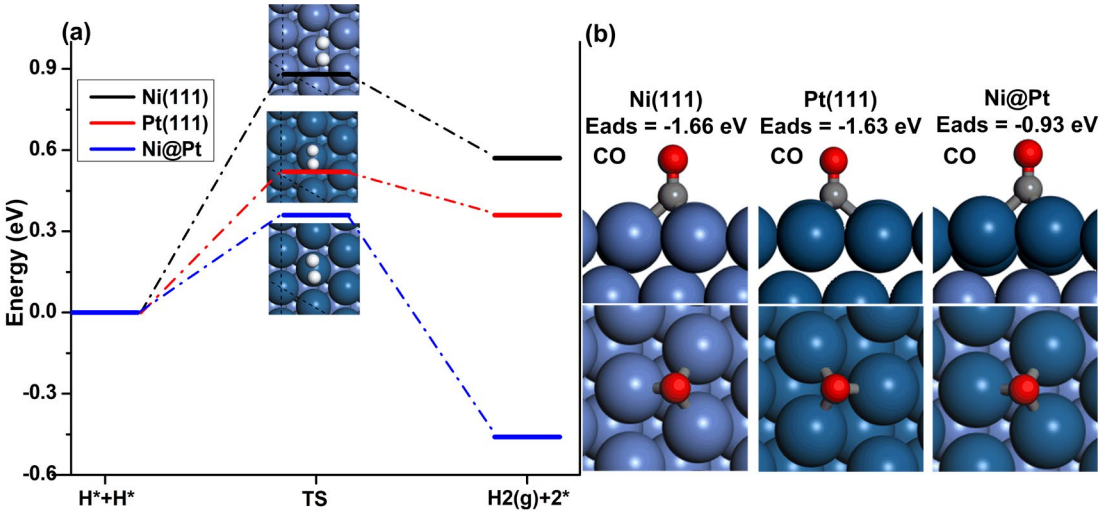

Fig. 5. (a) Energy profiles for H_2 formation and (b) CO adsorption on Ni(111), Pt(111) and Ni@Pt.

3.3.7 Reaction pathways

The dependence of the reaction pathways has been investigated by analyzing the free energy profiles of various pathways. There are many possible reaction pathways, which can be classified into the activation of CH_x (x = 2-4) by direct dissociation, O* and OH* activation. Here we screen out the possible reaction pathways first by a simple analysis of the

activation energies of the corresponding elemental steps, as shown in Fig. 6. We found that on Ni(111), direct dissociation way is most favorable in three dehydrogenation steps, while on Ni@Pt, OH*-assisted CH_4 activation into CH proceeds more easily in three dehydrogenation steps. On Pt(111), for the first C–H bond activation, OH-assisted way presents the lowest energy barrier, while for the second and third C–H bond activation, direct dehydrogenation way shows a little bit lower energy barrier. In addition, OH* assisted activation of CH_x is energetically more favorable compared to O* assisted activation. Therefore, the O* assisted activation pathways were excluded in the next analysis.

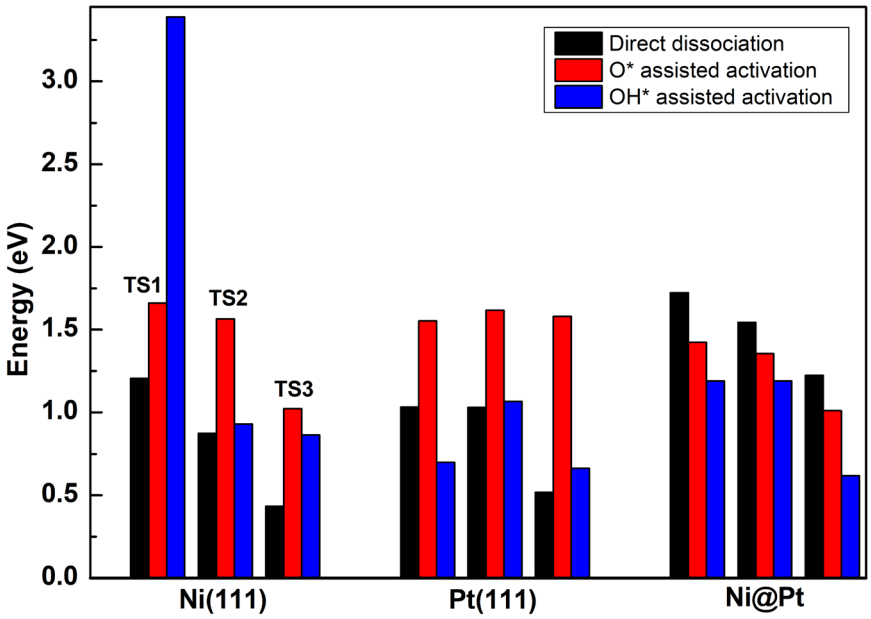

Fig. 6. Energy barriers for CH_4 activation into CH of three pathways. TS1: CH_4 activation; TS2: CH_3 activation; and TS3: CH_2 activation.

The rate-determining step in the methane steam reforming on metal surface is still in debate and unclear. CH oxidation by OH* [20] and methane dissociation [54,60,61] have been often proposed as the rate-determining steps (*RDS*). It has been reported that the rate-determining step depends on the temperatures [62] and pressures [12]. It is generally agreed by DFT [60] and experimental results [54] that the methane dissociation is the rate-determining step at relatively high temperatures. In addition, experimental observation demonstrated that the forward rate is first order with respect to the methane partial pressure

and that it does not depend on the partial pressure of water in *SRM*, and C–H bond activation is the sole kinetically relevant step [54]. The free energy profiles of the reaction pathway based on the direct dissociation of CH_x and following surface oxidation of CH were plotted in Fig. 7. The highest free energy located at the step of H_2O dissociation suggesting H_2O activation as the *RDS*, which is contrast to the experimental observation. In addition, the results from the free energy profiles suggest that the rate-determining step depends on the steam activation. On metal surfaces in Fig. 7, activation of steam has a large energy barrier mostly caused by an entropy change.

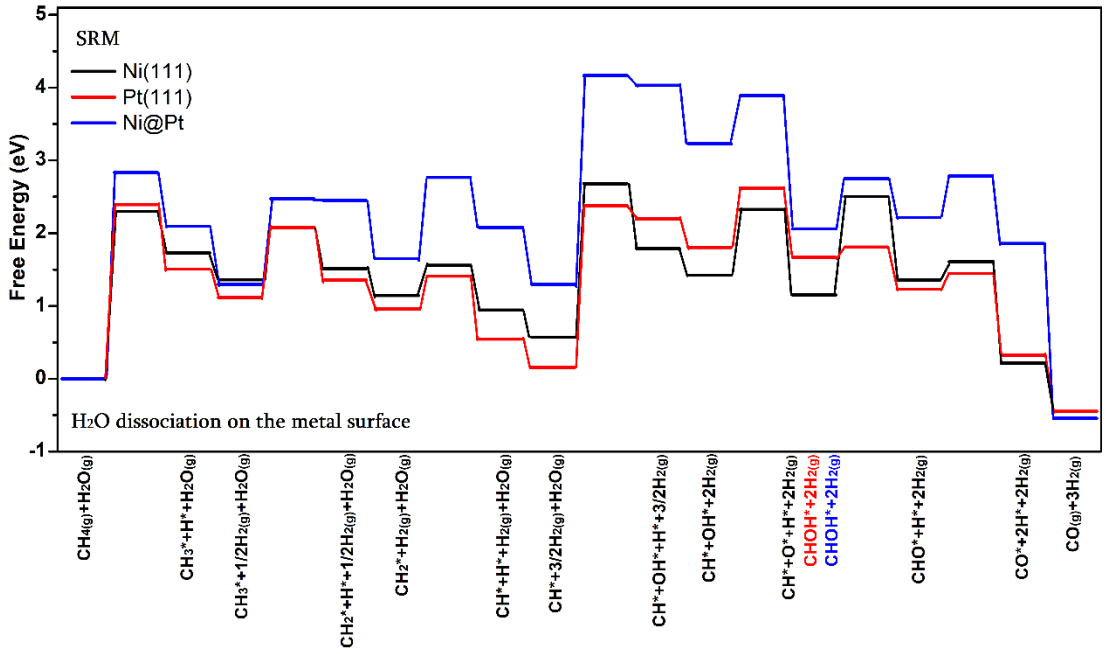

Fig. 7. Free energy landscape and dominant reaction mechanisms in SRM on Ni(111), Pt(111) and Ni@Pt, H_2O dissociation on the metal surface. Reaction conditions: P_{CH4} = 0.5 bar, P_{H2O} = 0.5 bar, T = 1000 K.

It should be noticed that water dissociation is more likely to proceed on the support instead of metal surface [63–66]. In addition, DFT studies on water dissociation over TiO_2 [64], Al_2O_3 [65], and MgO [66] surface showed significantly lower barriers (< 0.3 eV). Moreover, surface area of support is relatively large, it is expected that OH* is rich on the support, which could serve as a resource immigrating to metal surface. However, this important experimental observation has not been taken into account in any DFT assisted mechanistic studies. Although it might be a small free energy for activation of steam on

support and surface diffusion to metal, here we simplify and treat it as an extreme case of zero entropy change of steam activation on metals. It means that OH* on metal surface is possibly equilibrated with OH* on the support, and there is no entropy changes.

By the assumption of steam activation on supports and zero entropy change, the free energy profiles of reaction pathways of methane direct dissociation and OH* assisted activation in *SRM* on three metal surfaces at 1000 K, are plotted in Fig. 8. In the CH_4 direct dissociation pathway (Fig. 8a), the oxidation of CH has priority over CH decomposition on all three surfaces, according to the previous study in this paper. Thus, the dominant pathway for CH oxidation to form CO follows the mechanisms: on Ni(111), CH* + O* → CHO* + * → CO* + H*; on Pt(111) and Ni@Pt, CH* + OH* + *→ CHOH* + 2* → CHO* + H* +* → CO* + 2H*. For Ni(111) and Pt(111) surfaces, the highest the free energy is the step of CH_4 dissociation, it suggests that the CH_4 adsorptive dissociation is the rate determining step, which has been confirmed in our experimental work [67], the H_2 reaction order is close to zero. It is interesting to note that the rate-determining step has been changed from CH oxidation to CH_4 adsorptive dissociation when the steam activation changed from the metal surface to supports. It reveals that the support could play an important role in determining the *RDS*.

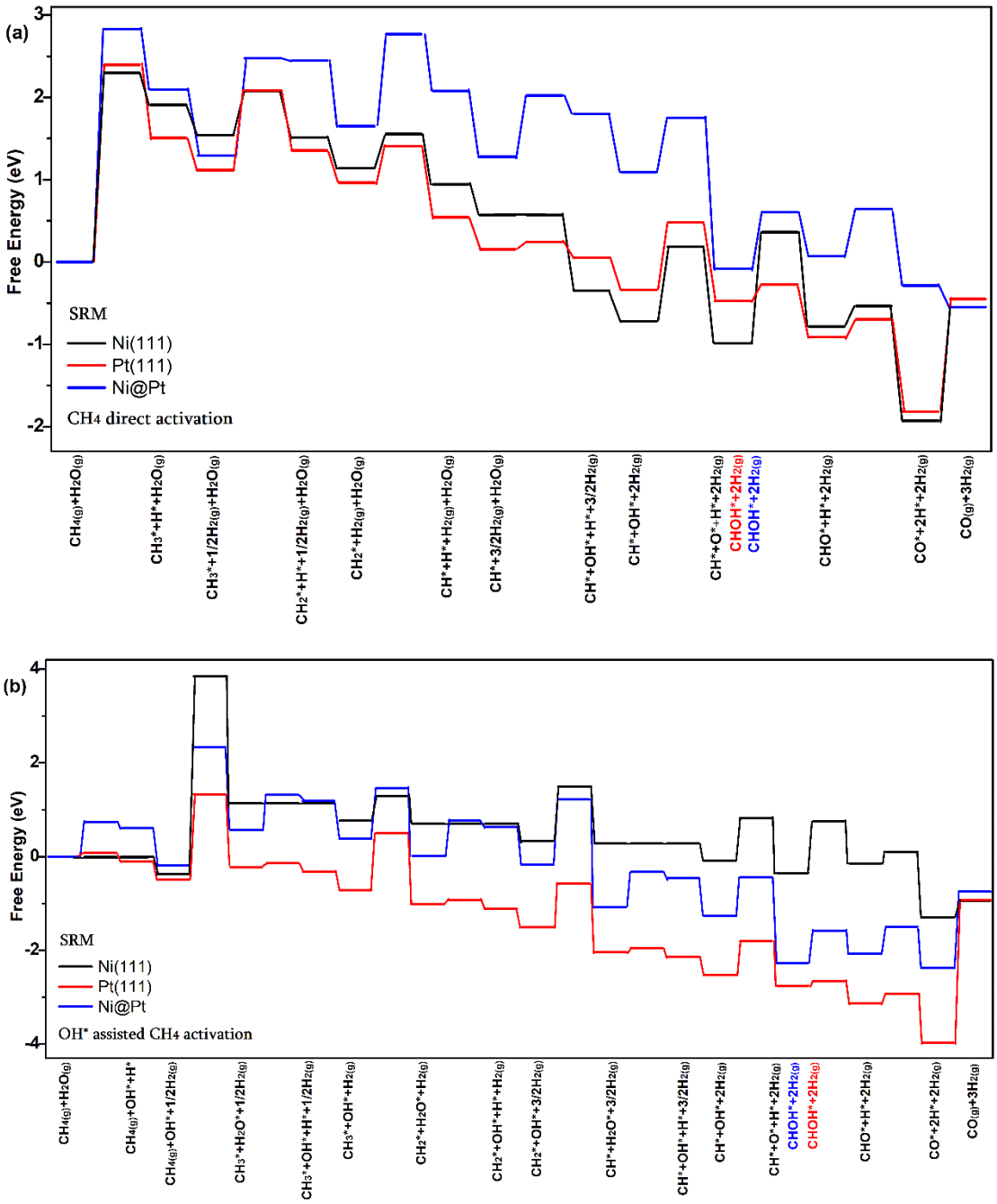

Fig. 8. Free energy landscape and dominant reaction mechanisms in *SRM* on three surfaces: (a) CH_4 direct dissociation way; and (b) OH-assisted CH_4 activation way. Reaction conditions: P_{CH4} = 0.5 bar, P_{H2O} = 0.5 bar, T = 1000 K.

For OH-assisted CH_x activation pathway (Fig. 8b), the OH* assisted methane dissociation on Ni(111) has a much higher maximum free energy, but a lower maximum free energy on Pt(111) compared to methane direct dissociation pathways. It suggests that the OH* assisted reaction pathways is dominating on Pt(111) and methane direct dissociation is

dominating on Ni(111). OH* assisted methane dissociation is the rate-determining step on both surfaces. On Ni@Pt surface, the free energy for the reaction pathway of direct dissociation of CH_x (Fig. 8a) is significantly higher than the OH* assisted pathway (Fig. 8b). It suggests that the OH* assisted CH_x activation pathway is the dominating one on Ni@Pt surface.

We have obtained the dominant reaction routes on three catalysts, as depicted in Fig. 9. It is clearly seen that CH_4 activation proceeds in direct dissociation way on Ni, while OH-assisted CH_4 activation acts the dominant way on Pt and Ni@Pt.

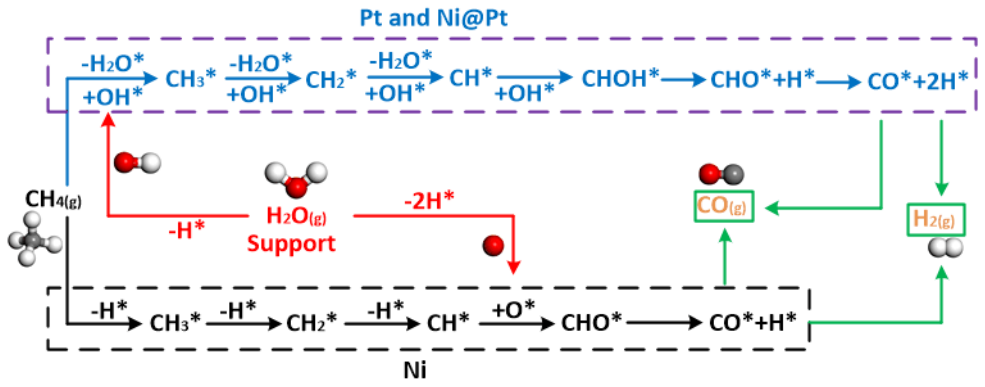

Fig. 9. Dominant reaction routes on three surfaces.

3.4 Experimental study

3.4.1 Characterization of catalysts

***XPS*:** It is noteworthy that Pt electronegative elements in relation to Ni and hence Pt atoms could produce an electron withdrawing effect from the neighboring Ni atoms bringing about the polarization of the Pt–Ni bonds between first layer and second layer in the bimetallic particle, which would cause a negative shift in the binding energy of the $4f_{5/2}$ signal of the Pt^0. The XPS spectrum (Fig. 10a) for the bimetallic Ni@Pt catalysts clearly shows one peak assigned to $Pt4f_{5/2}$ spectra of metallic Pt, in which its binding energy shifted to the lower level of 73.9 eV. Binding energy of $Ni2p_{1/2}$ in Ni@Pt catalysts shifted to the higher level. It clearly indicates charge transfer from Pt to Ni in the core-shell structured Ni@Pt, which is in good agreement with DFT prediction that the core-shell Ni@Pt catalyst

modified the surface Pt electron density and shifted d-band center away from Fermi level compared with Ni(111). Moreover, it is evidently observed of suppression of $Ni2p_{1/2}$ peaks in Ni@Pt catalysts (Fig. 10b) when second metal Pt deposited on the Ni surface by replacing Ni, suggesting Pt is mostly on the particle surface.

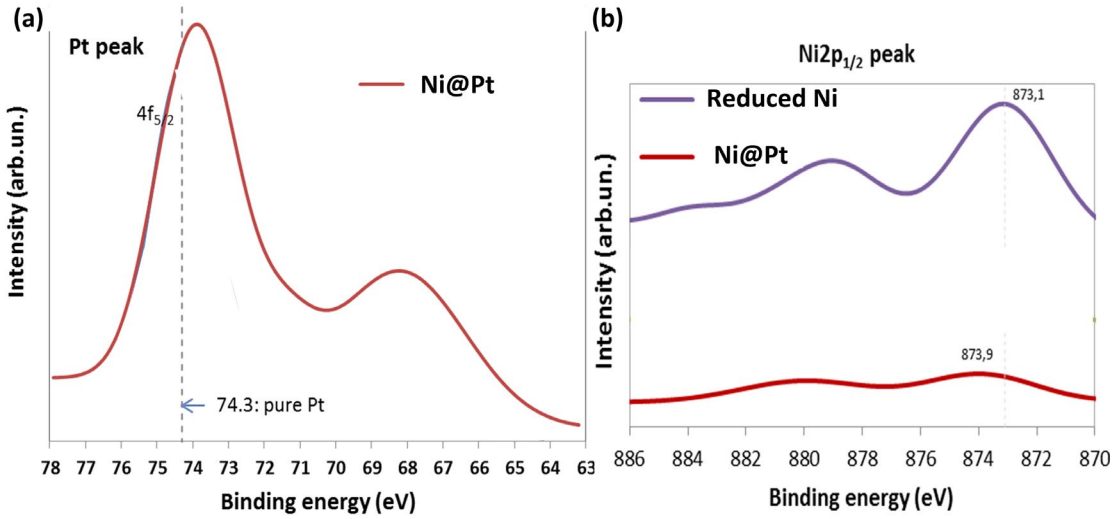

Fig. 10. XPS spectra of the Ni@Pt catalyst (a) $Pt4f_{5/2}$; and (b) $Ni2p_{1/2}$.

***H_2 chemisorption and TEM*:** The active surface area of Ni and Ni@Pt catalysts was calculated from the quantity of hydrogen uptake. Compared with pure Ni catalysts, addition of Pt into Ni-HT catalyst causes a decreasing trend in the amount of hydrogen chemisorbed, thus showing a decrease in metallic surface area, the details are provided in Table 3.

Table 3

Metallic surface area from H_2 chemisorption and lattice distance from TEM images and DFT calculations.

Catalyst	Metallic Surface Area [m^2/g_{metal}]	TEM Lattice distance [nm]	DFT Lattice distance [nm]
Ni	40.74	0.200	0.216
Ni@Pt	29.96	0.214	0.225
Pt		0.230♣	0.239

♣: Ref [68].

In addition, Fig. 11 shows the TEM images of Ni and Ni@Pt catalysts. Specifically, Fig. 11a and 11b indicate that the average particle size of Ni catalysts is around 8.10 nm, and Fig. 11d and 11e suggest that the average particle size of Ni@Pt catalysts is around 8.80 nm,

which is in good agreement with that the metallic surface area decrease from Ni to Ni@Pt. In addition, fringes of 0.200 nm [69] of metallic Ni^0 and 0.214 nm of Ni@Pt were attributed to (111) planes of Ni and Ni@Pt catalysts, as depicted in Fig. 11c and 11f, respectively. In addition, it can be concluded that the lattice distance of Ni@Pt is between monometallic ones, and the results from TEM images and DFT models are in good agreement. Combined lattice distance from TEM images and DFT models and peak shift of XPS spectrum, it indicates that we have successfully synthesized Ni@Pt catalysts.

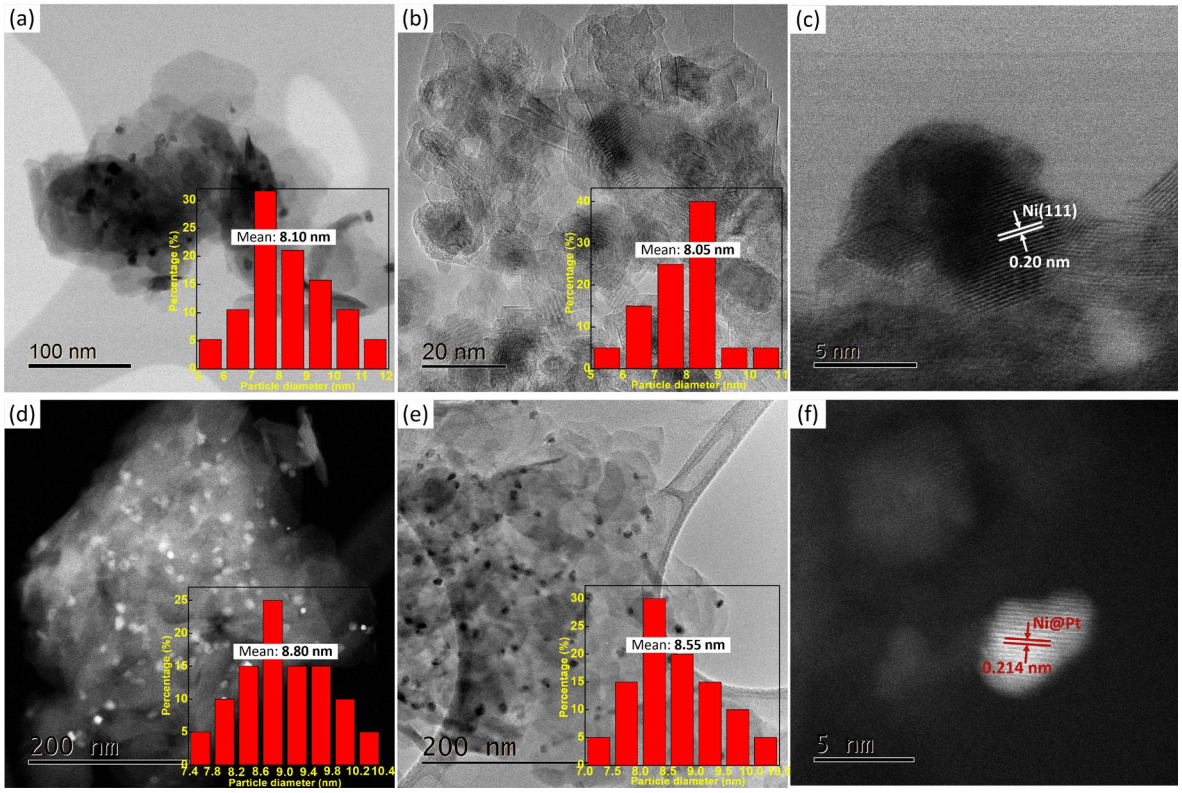

Fig. 11. TEM images of Ni (a) fresh sample, (b) reduced sample, and (c) Ni surface lattice distance; and Ni@Pt (d) (e) reduced sample, and (f) Ni@Pt surface lattice distance.

3.4.2 Kinetic study of SRM on Ni and Ni@Pt catalysts

The turnover frequency TOF_{Exp} is calculated from the initial reaction rate (r_i) and Ni dispersion (D), as shown below:

$$r = \frac{X \cdot F}{W} = \frac{X \cdot F}{W \cdot 22414 \cdot 60} \cdot \frac{273.15}{298.15} (\mathrm{mol \cdot s^{-1} \cdot g_{cat}^{-1}}) \quad (5)$$

$$TOF_{Exp} = \frac{r_i M_{Ni}}{f_{Ni} D} \quad (6)$$

where X is the conversion, F is the gas flow rate, W is the catalysts weight, M_{Ni} is the molecular weight of Ni, f_{Ni} is the Ni weight fraction of the catalysts. The dispersion D was estimated based on the surface area of metal measured by hydrogen chemisorption.

In addition, based on previous DFT calculations and G plot, we select the lowest energy pathway for SRM on Ni and Ni@Pt, namely CH_4 direct activation way and OH-assisted activation way, respectively, the temperatures of 773 K, 798 K, 823 K and 848 K applied for kinetic relevant steps to compare with the experiment results. The turn over frequency could also be calculated as follows based on the highest point of G plot, this point is determined by TS of CH_4—CH_3+H for Ni and CH_4+OH—CH_3+H_2O for Ni@Pt in this paper, which due to CH_4 activation step is the *RDS*:

$$TOF_{DFT} = \frac{k_b T}{h} \exp(\frac{-\Delta G}{RT}) P_{CH4} P_{H2}^{n} \theta^{*2} \quad (7)$$

where k_b is the Boltzmann constant, T is the reaction temperature, h is the Planck constant, ΔG is the highest point of the G plot in Fig.12, R is the gas constant, P_{CH4} is the partial pressure of CH_4, and P_{H2} is the partial pressure of H_2, due to the first C–H bond activation is regarded as the *RDS*, here reaction order for H_2 n = 0. The experiments are performed at relatively low pressures and high temperatures, and site vacancy (θ*) is assumed close to 1.

Fig. 12 shows the Arrhenius plot and effective activation energy generated from experimental and DFT study over Ni and Ni@Pt. It can be clearly seen that two Arrhenius plots drawn from experimental and DFT studies are almost parallel on both Ni and Ni@Pt catalysts. The measured experimental effective activation energy of 104.2 kJ/mol for *SRM* on hydrotalcite-derived Ni catalysts in present work agrees well with the reported values of 103.6 kJ/mol at Ni/Mg(Al)O [67] and 102 kJ/mol at Ni/Al_2O_3 [54]. The effective activation energy calculated from G plot here (108.2 kJ/mol) is rather in good agreement with the

experimental one (104.2 kJ/mol). Moreover, the effective activation energy is estimated from DFT assisted kinetic analysis (112. 2 kJ/mol) is also consistent with the experimental value (110.9 kJ/mol) on the Pt@Ni catalysts.

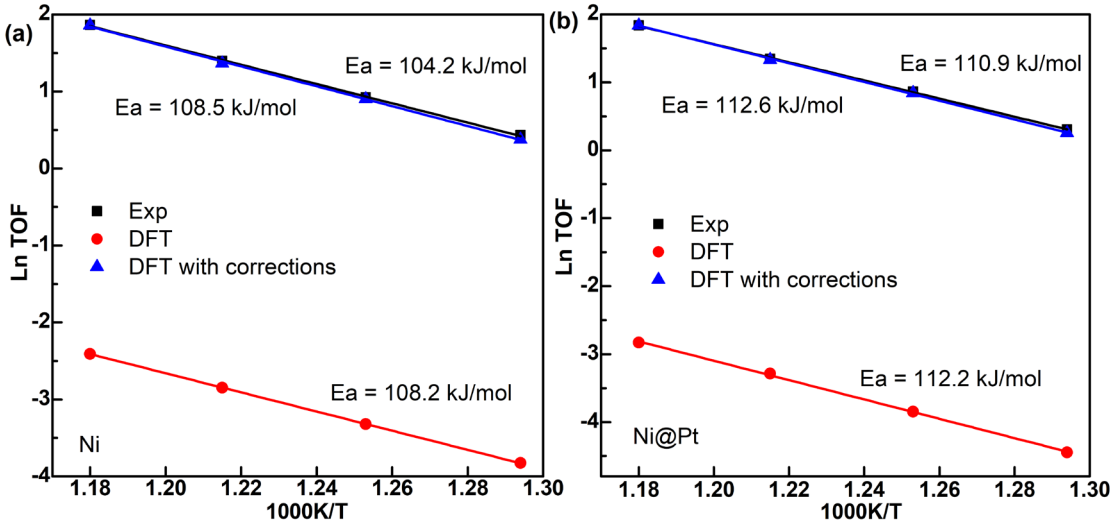

Fig. 12. Arrhenius plot and apparent activation energy generated from experiment and DFT over (a) Ni and (b) Ni@Pt. Reaction conditions: S/C=3.5, CH_4/H_2=1.0, W/F_0 between 0.018 and 0.037 mol.g. s^{-1}.

The pre-exponential factors were obtained from the Arrhenius plots as shown in Table 4 based on the DFT assisted kinetic analysis. The effective entropy changes was also estimated from the pre-exponential factors based on the transition state theory. It is clearly seen (Table 4) that effective entropy change on Ni is larger than that on Ni@Pt. The effective entropy change is mostly related to the change between the transition state of methane activation and the gas phase methane. The smaller effective entropy change indicates the weaker adsorption of the transition state complex on Ni@Pt compared to Ni, which could be attributed to that the *d*-band center of Ni@Pt is more far away from Fermi-level than that of Ni(111). It results also in a slightly higher effective activation energy on Ni@Pt than Ni. The estimated pre-exponential factors from DFT calculation (Table 4) are similar to the reported value [70]. The compensation between the entropy change and the effective activation energy makes Ni@Pt without significant scarifying activity (TOF) compared to Ni.

Table 4

Entropy changes and pre-exponential factor before and after corrections at 773 K.

Catalyst	Entropy change ΔS [J/(mol·K)]	Pre-exponential factor [s^{-1}]	Entropy change after corrections ΔS [J/(mol·K)]	Pre-exponential factor after correction [s^{-1}]
Ni	- 109.80	2.96×10^{7}	- 75.21	1.90×10^{9}
Ni@Pt	- 82.76	7.65×10^{8}	- 42.82	9.33×10^{10}

In addition, such good agreement between DFT prediction and experimental effective activation energy could support the different mechanisms proposed by DFT calculations, namely CH_4 activation on Ni, while OH* assisted CH_4 activation on Ni@Pt. However, there is obvious deviation of the DFT predicted TOF from the experimental ones, but the two curves in Arrhenius plots are parallel. We tune the effective entropy change as a sole parameter to fit the experimental TOSs. The corrected effective entropies for both catalysts are summarized in Table 4. The new free energy profiles after effective entropy corrections are shown in Fig. S10. The corrected kinetic model describes the experimental data satisfactorily. The corrected effective entropy is about 34 and 40 J/(mol•K) smaller than DFT predicted entropy for Ni and Ni@Pt, respectively. It should be noticed that the DFT calculation is only on ideal surface of Ni(111). Although the particle size is relatively large and Ni(111) surface is dominating, Ni(100) and Ni(211) could also contribute to the reaction. The correction of effective entropy change might include the contribution of different surfaces.

3.4.3 Coke formation rate on Ni and Ni@Pt catalysts

Moreover, we have performed the temperature programmed oxidation (TPO) analysis (Fig. S11) for both Ni and Ni@Pt samples to obtain the coke formation rate. The results shows that the total amount of coke formation for Ni after 4.5 hrs running is around 20 wt% of initial catalysts, while for Ni@Pt after 5.1 hrs running it is decreasing 13 wt%. Due to the

carbon formation is very low, here we assume that total amount of coke increases linearly as time goes by. Therefore, the coking rate for Ni catalyst is around 0.044 $mg_{coke}/(mg_{cat}•h)$, while for Ni@Pt it is decreasing to 0.026 $mg_{coke}/(mg_{cat}•h)$, thus Ni@Pt catalyst shows the better anti-carbon formation ability compared to monometallic Ni, which is in good agreement with our DFT predictions in section 3.3.5.

4. Conclusions

The mechanisms of steam reforming on Ni, Pt and single layer core-shell structured Pt@Ni catalysts are examined by combining DFT calculations, experimental kinetic study and DFT assisted kinetic analysis. The monolayer core-shell structured Ni@Pt catalyst was successfully prepared by surface redox reaction between surface Ni and Pt cations. We demonstrated experimentally core-shell structured Ni@Pt significantly lowered carbon formation without reducing very much the reaction rate. The DFT results revealed that introducing Pt atoms into Ni surface forming Ni@Pt makes the curves of PDOS broad and *d*-band center shifted away from Fermi level compared with Ni(111) and Pt(111), which could lead to weakening the binding strength between absorbates and metal surface. It is found that CH decomposition into C + H barrier on the Ni@Pt remarkably increases to around 1.979 eV. Furthermore, Ni@Pt provides much less energy-demanding pathways for both CH and C oxidation. Therefore, CH is much energetically favored to be oxidized rather than cracking into carbon on this surface, meanwhile, Ni@Pt is beneficial for carbon elimination and shows promising anti-carbon formation performance. In addition, mechanistic study reveal a crucial role of steam activation on supports in determining favorable reaction pathways. It indicated that the mechanism with steam activated on support is in good agreement with the experimental observation. Among three methane activation pathways examined, CH_4 direct dissociation is energetically favorable on Ni, while OH* assisted methane activation is the

dominating reaction pathway on Pt and Ni@Pt. In addition, a DFT assisted kinetic analysis is introduced to efficiently elucidate the rate-demining step and directly estimate the reaction rate from the free energy profile based DFT calculated energetics. The estimated effective activation energy is in good agreement with experimental ones on both Ni and Ni@Pt. The approach introduced in this contribution can efficiently improve the model predictions to achieve excellent agreement with experimentally measured kinetic data.

Acknowledgment

The authors would like to thank the Project Supported by Graduate Scientific Research and Innovation Foundation of Chongqing, China (Grant No. CYB16022), China Scholarship Council (Grant No. 201606050054), and Department of Chemical Engineering, Norwegian University of Science and Technology, Norway. The computational calculations provided by Notur project (www.notur.no) is highly acknowledged (nn4685k).

References

[1] F. Che, J.T. Gray, S. Ha, J.S. McEwen, Improving Ni catalysts using electric fields: A DFT and experimental study of the methane steam reforming reaction, ACS Catal. 7 (2017) 551–562.

[2] Niu, J., Chemical Engineering Journal (2018), https://doi.org/10.1016/j.cej.2018.08.149.

[3] X. Feng, J. Yang, X. Duan, Y. Cao, B. Chen, W. Chen, D. Lin, G. Qian, D. Chen, C. Yang, X. Zhou, Enhanced catalytic performance for propene epoxidation with H_2 and O_2 over bimetallic Au−Ag/uncalcined titanium silicate-1 catalysts, ACS Catal. 8 (2018) 7799–7808.

[4] H. Lee, D.-H. Lee, Y.-H. Song, W.C. Choi, Y.-K. Park, D.H. Kim, Synergistic effect of non-thermal plasma–catalysis hybrid system on methane complete oxidation over Pd-based catalysts, Chem. Eng. J. 259 (2015) 761–770.

[5] P. Stefanov, S. Todorova, A. Naydenov, B. Tzaneva, H. Kolev, G. Atanasova, D. Stoyanova, Y. Karakirova, K. Aleksieva, On the development of active and stable Pd–Co/γ-Al2O3 catalyst for complete oxidation of methane, Chem. Eng. J. 266 (2015) 329–338.

[6] G. Pantaleo, V. LaParola, F. Deganello, R.K. Singha, R. Bal, A.M. Venezia, Ni/CeO2 catalysts for methane partial oxidation: Synthesis driven structural and catalytic effects, Appl. Catal. B: Environ. 189 (2016) 233–241.

[7] Q. Li, T. Wang, Y. Liu, D. Wang, Experimental study and kinetics modeling of partial oxidation reactions in heavily sooting laminar premixed methane flames, Chem. Eng. J. 207–208 (2012) 235–244.

[8] R.C. Cataphan, A.A. M. Oliveira, Y. Chen, D.G. Vlachos, DFT study of the water−gas shift

reaction and coke formation on Ni(111) and Ni(211) surfaces, J. Phys. Chem. C 116 (2012) 20281–20291.

[9] S.D. Angeli, L. Turchetti, G. Monteleone, A.A. Lemonidou, Catalyst development for steam reforming of methane and model biogas at low temperature, Appl. Catal. B: Environ. 181 (2016) 34–46.

[10]D. Pakhare, J. Spivey, A review of dry (CO_2) reforming of methane over noble metal catalysts, Chem. Soc. Rev. 43 (2014) 7813−7837.

[11]F. Polo-Garzon, M. He, D.A. Bruce, *Ab initio* derived reaction mechanism for the dry reforming of methane on Rh doped pyrochlore catalysts, J. Catal. 333 (2016) 59–70.

[12]C. Fan, Y.A Zhu, M.L. Yang, Z.J. Sui, X.G. Zhou, D. Chen, Density functional theory-assisted microkinetic analysis of methane dry reforming on Ni catalyst, Ind. Eng. Chem. Res. 54 (2015) 5901−5913.

[13]Y. Kathiraser, U. Oemar, E.T. Saw, Z. Li, S. Kaw, Kinetic and mechanistic aspects for CO_2 reforming of methane over Ni based catalysts, Chem. Eng. J. 278 (2015) 62–78.

[14]Z. Wang, X.M. Cao, J. Zhu, P. Hu, Activity and coke formation of nickel and nickel carbide in dry reforming: A deactivation scheme from density functional theory, J. Catal. 311 (2014) 469–480.

[15]J. Ni, L. Chen, J. Lin, S. Kawi, Carbon deposition on borated alumina supported nano-sized Ni catalysts for dry reforming of CH_4, Nano Energy 1 (2012) 674–686.

[16]M. Maestri, D.G. Vlachos, A. Beretta, G. Groppi, E. Tronconi, Steam and dry reforming of

methane on Rh: Microkinetic analysis and hierarchy of kinetic models, J. Catal. 259 (2008) 211–222.

[17]J. Niu, X. Du, J. Ran, R. Wang, Dry (CO_2) reforming of methane over Pt catalysts studied by DFT and kinetic modeling, Appl. Surf. Sci. 376 (2016) 79–90.

[18]W. Yu, M.D. Porosoff, J.G. Chen, Review of Pt-based bimetallic catalysis: From model surfaces to supported catalysts, Chem. Rev. 112 (2012) 5780−5817.

[19]M.D. Marcinkowski, M.T. Darby, J. Liu, J.M. Wimble, F.R. Lucci, S. Lee, A. Michaelides, M. Flytzani-Stephanopoulos, M. Stamatakis, E. C.H. Sykes, Nat. Chem. 10 (2018) 325−332.

[20]S. Li, J. Gong, Strategies for improving the performance and stability of Ni-based catalysts for reforming reactions, Chem. Soc. Rev. 43 (2014) 7245−7256.

[21]S.T. Hunt, Y. Román-Leshkov, Principles and methods for the rational design of core−shell nanoparticle catalysts with ultralow noble metal loadings, Acc. Chem. Res. 51 (2018) 1054−1062.

[22]Z. Li, M. Li, Z. Bian, Y. Kathiraser, S. Kawi, Design of highly stable and selective core/yolk–shell nanocatalysts—A review, Appl. Catal. B: Environ. 188 (2016) 324–341.

[23]Z. Li, L. Mo, Y. Kathiraser, S. Kawi, Yolk−satellite−shell structured Ni−yolk@Ni@SiO_2 nanocomposite: Superb catalyst toward methane CO_2 reforming reaction, ACS Catal. 4 (2014) 1526–1536.

[24]M.B. Gawande, A. Goswami, T. Asefa, H. Guo, A.V. Biradar, D.L. Peng, R. Zboril, R.S. Varma, Core–shell nanoparticles: synthesis and applications in catalysis and electrocatalysis,

Chem. Soc. Rev. 44 (2015) 7540−7590.

[25]Y. Huang, J. Du, C. Ling, Z. Qin, J. Ling, T. Zhou, S. Wang, Methane dehydrogenation on Au/Ni surface alloys–a first-principles study, Catal. Sci. Technol. 3 (2013) 1343–1354.

[26]P. Bothra, S.K. Pati, Improved catalytic activity of rhodium monolayer modified nickel (110) surface for the methane dehydrogenation reaction: a first-principles study, Nanoscale 6 (2014) 6738–6744.

[27]Y. Zhao, S. Li, Y. Sun, Theoretical study on the dissociative adsorption of CH_4 on Pd-doped Ni surfaces, Chinese J. Catal. 34 (2013) 911–922.

[28]H. Liu, R. Yan, R. Zhang, B. Wang, K. Xie, A DFT theoretical study of CH_4 dissociation on gold-alloyed Ni(111) surface, J. Nat. Gas Chem. 20 (2011) 611–617.

[29]M. Zhang, K. Yang, X. Zhang, Y. Yu, Effect of Ni(111) surface alloying by Pt on partial oxidation of methane to syngas: A DFT study, Surf. Sci. 630 (2014) 236–243.

[30]C. Fan, Y.A. Zhu, Y. Xu, Y. Zhou, X.G. Zhou, D. Chen, Origin of synergistic effect over Ni-based bimetallic surfaces: A density functional theory study, J. Chem. Phys. 137 (2012) 014703.

[31]D. Hibbitts, M. Neurock, Promotional effects of chemisorbed oxygen and hydroxide in the activation of C–H and O–H bonds over transition metal surfaces, Surf. Sci. 650 (2016) 210–220.

[32]B.N. Zope, D. Hibbitts, M. Neurock, R.J. Davis, Reactivity of the gold/water interface during selective oxidation catalysis, Science 330 (2010) 74–78.

[33]D. Hibbitts, M. Neurock, Influence of oxygen and pH on the selective oxidation of ethanol on Pd catalysts, J. Catal. 299 (2013) 261–271.

[34]M.L. Yang, C. Fan, Y.A. Zhu, Z.J. Sui, X.G. Zhou, D. Chen, Selective oxidation of hydrogen in the presence of propylene over Pt-based core–shell nanocatalysts, J. Phys. Chem. C 119 (2015) 21386–21394.

[35]Y.Z. Chen, Q. Xu, S.H. Yu, H.L. Jian, Tiny Pd@Co core–shell nanoparticles confined inside a metal–organic framework for highly efficient catalysis, Small, 11 (2015) 71–76.

[36]A.V. Ruban, H.L. Skriver, J.K. Nørskov, Surface segregation energies in transition-metal alloys, Phys. Rev. B 59 (1999) 15990–16000.

[37]L.L. Wang, D.D. Johnson, Predicted trends of core−shell preferences for 132 late transition-metal binary-alloy nanoparticles, J. Am. Chem. Soc. 131 (2009) 14023–14029.

[38]J. Li, E. Croiset, L. Ricardez-Sandoval, Effect of carbon on the Ni catalyzed methane cracking reaction: A DFT study, Appl. Surf. Sci. 311 (2014) 435–442.

[39]Y. Chen, D.G. Vlachos, Density functional theory study of methane oxidation and reforming on Pt(111) and Pt(211), Ind. Eng. Chem. Res. 51 (2012) 12244−12252.

[40]M.C. Payne, M.P. Teter, D.C. Allan, T.A. Arias, J.D. Joannopoulos, Iterative minimization techniques for ab initio total-energy calculations: molecular dynamics and conjugate gradients, Rev. Mod. Phys. 64 (1992) 1045–1097.

[41]J. Wellendorff, K.T. Lundgaard, A. Mogelhoj, V. Petzold, D.D. Landis, J.K. Norskov, T. Bligaard, K.W. Jacobsen, Density functionals for surface science: Exchange-correlation model development with Bayesian error estimation, Phys. Rev. B 85 (2012) 235149.

[42]F. Studt, F. Abild-Pedersen, J. Varley, J. Nørskov, CO and CO_2 hydrogenation to methanol

calculated using the BEEF-vdW functional, Catal. Lett. 143 (2013) 71–73.

[43]Y. Qi, C. Ledesma, J. Yang, X. Duan, Y.A. Zhu, A. Holmen, D. Chen, Adsorption energy-driven carbon number-dependent olefin to paraffin ratio in cobalt-catalyzed Fischer-Tropsch synthesis, J. Catal. 349 (2017) 110–117.

[44]J.P. Perdew, K. Burke, M. Ernzerhof, Generalized gradient approximation made simple, Phys. Rev. Lett. 77 (1996) 3865–3868.

[45]H.J. Monkhorst, J.D. Pack, Special points for Brillouin-zone integrations, Phys. Rev. B 13 (1976) 5188–5192.

[46]G. Henkelman, H. Jonsson, A dimer method for finding saddle points on high dimensional potential surfaces using only first derivatives, J. Chem. Phys. 111 (1999) 7010–7022.

[47]Y.A. Zhu, D. Chen, X.G. Zhou, W.K. Yuan, DFT studies of dry reforming of methane on Ni catalyst, Catal. Today 148 (2009) 260–267.

[48]H. Liu, D. Wierzbicki, R. Debek, M. Motak, T. Grzybek, P.D. Costa, M.E. Gálvez, La-promoted Ni-hydrotalcite-derived catalysts for dry reforming of methane at low temperatures, Fuel 182 (2016) 8–16.

[49]J. Niu, J. Ran, X. Du, W. Qi, P. Zhang, L. Yang, Effect of Pt addition on resistance to carbon formation of Ni catalysts in methane dehydrogenation over Ni-Pt bimetallic surfaces: A density functional theory study, Molecular Catalysis 434 (2017) 206–218.

[50]J. Li, E. Croiset, L. Ricardez-Sandoval, Effect of carbon on the Ni catalyzed methane cracking reaction: A DFT study, Appl. Surf. Sci. 311 (2014) 435–442.

[51]S. Nave, B. Jackson, Methane dissociation on Ni(111) and Pt(111): Energetic and dynamical studies, J. Chem. Phys. 130 (2009) 054701.

[52]M. García-Diéguez, I.S. Pieta, M.C. Herrera, M.A. Larrubia, L.J. Alemany, Nanostructured Pt- and Ni-based catalysts for CO_2-reforming of methane, J. Catal. 270 (2010) 136–145.

[53]M. García-Diéguez, E. Finocchio, M.Á. Larrubia , L.J. Alemany, G. Busca, Characterization of alumina-supported Pt, Ni and PtNi alloy catalysts for the dry reforming of methane, J. Catal. 274 (2010) 11–20.

[54]J.M. Wei, E. Iglesia, Isotopic and kinetic assessment of the mechanism of reactions of CH_4 with CO_2 or H_2O to form synthesis gas and carbon on nickel catalysts, J. Catal. 224 (2004) 370–383.

[55]J. Niu, J. Ran, Z. Ou, X. Du, R. Wang, W. Qi, P. Zhang, CO_2 dissociation over Pt_xNi_{4-x} bimetallic clusters with and without hydrogen sources: A density functional theory study, J. CO_2 Util. 16 (2016) 431–441.

[56]J. Ko, B.K Kim, J.W. Han, Density functional theory study for catalytic activation and dissociation of CO_2 on bimetallic alloy surfaces, J. Phys. Chem. C 120 (2016) 3438–3447.

[57]L.Y. Gan, R.Y. Tian, X.B. Yang, H.D. Lu, Y.J. Zhao, Catalytic reactivity of CuNi alloys toward H_2O and CO dissociation for an efficient water–gas shift: A DFT study, J. Phys. Chem. C 116 (2012) 745–752.

[58]G. Psofogiannakis, A. St-Amant, M. Ternan, Methane oxidation mechanism on Pt(111): A cluster model DFT study, J. Phys. Chem. B 110 (2006) 24593–24605.

[59]R. Zhang, X. Guo, B. Wang, L. Ling, Insight into the effect of CuNi(111) and FeNi(111)

surface structure and second metal composition on surface carbon elimination by O or OH: A comparison study with Ni(111) surface, J. Phys. Chem. C 119 (2015) 14135–14144.

[60]H.S. Bengaard, J.K. Nørskov, J. Sehested, B.S. Clausen, L.P. Nielsen, A.M. Molenbroek, J.R. Rostrup-Nielsenb, Steam reforming and graphite formation on Ni catalysts, J. Catal. 209 (2002) 365–384.

[61]E. Nikolla, J. Schwank, S. Linic, Comparative study of the kinetics of methane steam reforming on supported Ni and Sn/Ni alloy catalysts: The impact of the formation of Ni alloy on chemistry, J. Catal. 263 (2009) 220–227.

[62]G. Jones, J.G. Jakobsen, S.S. Shim, J. Kleis, M.P. Andersson, J. Rossmeisl, F. Abild-Pedersen, T. Bligaard, S. Helveg, B. Hinnemann, J.R. Rostrup-Nielsen, I. Chorkendorff, J. Sehested, J.K. Nørskov, First principles calculations and experimental insight into methane steam reforming over transition metal catalysts, J. Catal. 259 (2008) 147–160.

[63]L. Foppa, T. Margossian, S.M. Kim, C. Müller, C. Coperet, K. Larmier, A. Comas-Vives, Contrasting the role of Ni/Al_2O_3 Interfaces in water−gas shift and dry reforming of methane, J. Am. Chem. Soc. 139 (2017) 17128–17139.

[64]J. Oviedo, R. Sánchez-de-Armas, M.A. San Miguel, J.F. Sanz, Methanol and water dissociation on TiO_2 (110): The role of surface oxygen, J. Phys. Chem. C 112 (2008) 17737–17740.

[65]V.A. Ranea, I. Carmichael, W.F. Schneider, DFT investigation of intermediate steps in the hydrolysis of α-Al_2O_3(0001), J. Phys. Chem. C 113 (2009) 2149–2158.

[66]R.S. Alvim, I. Borges, D.G. Costa, A.A. Leitão, Density-functional theory simulation of the

dissociative chemisorption of water molecules on the MgO(001) surface, J. Phys. Chem. C 116 (2012) 738–744.

[67]H. Wang, D.W. Blaylock, A.H. Dam, S.E. Liland, K.R. Rout, Y.A Zhu, W.H. Green, A. Holmen, D. Chen, Steam methane reforming on a Ni-based bimetallic catalyst: density functional theory and experimental studies of the catalytic consequence of surface alloying of Ni with Ag, Catal. Sci. Technol. 7 (2017) 1713–1725.

[68]Q.Fu, W.X. Li, Y. Yao, H. Liu, H.Y. Su, D. Ma, X.K. Gu, L. Chen, Z. Wang, H. Zhang, B. Wang, X. Bao, Science 328 (2010) 1141–1144.

[69]R.K. Singha, A. Shukla, A. Sandupatla, G. Deo, R. Bal, Synthesis and catalytic activity of a Pd doped Ni–MgO catalyst for dry reforming of methane, J. Mater. Chem. A 5 (2017) 15688–15699.

[70]D. Chen, R. Lødeng, H. Svendsen, A. Holmen, Hierarchical multiscale modeling of methane steam reforming reactions, Ind. Eng. Chem. Res. 50 (2011) 2600−2612.